

A detailed three-dimensional quantum study of the Li+FH reaction

G. A. Parker

Department of Physics and Astronomy, University of Oklahoma, Norman, Oklahoma 73019

A. Laganà and S. Crocchianti

Dipartimento di Chimica, Università di Perugia, Perugia, Italy

R. T Pack

Theoretical Division (T12, MS B268), Los Alamos National Laboratory, Los Alamos, New Mexico 87545

(Received 25 August 1994; accepted 12 October 1994)

Accurate quantum reactive scattering calculations in the full three-dimensional physical space have been carried out for the Li+FH reaction at zero total angular momentum using the adiabatically adjusting principal axis of inertia hyperspherical coordinate formalism. The procedures for fitting the potential energy surface, calculating the surface functions, and propagating the solutions in a coupled channel treatment are given and discussed. Features of the resulting reactive probability plots are analyzed, and simple explanations of a number of the quantum resonance and oscillatory features are found. © 1995 American Institute of Physics.

I. INTRODUCTION

The Li+FH→LiF+H reaction has several interesting features that make it an ideal prototype of the generic A+BC→AB+C reaction. The Li, F, and H masses provide one of the lightest three-different-atom reactive systems, the potential energy surface of the reaction has a noncollinear transition state, there are two potential wells and a barrier along the reaction path, and the reaction is classically endoergic but quantumly exoergic due to the difference in initial and final vibrational zero-point energies.

On the experimental side the Li+FH reaction has been extensively studied in crossed beams^{1,2} including studies in which the target molecule was oriented using electric fields.²

On the theoretical side, *ab initio* calculations of the potential energy surface have been performed,^{3,4} and the results of Ref. 4 have been fitted to different analytic forms.⁵⁻⁷ Both classical trajectory⁸⁻¹¹ and approximate quantum reactive scattering^{12,13} calculations have been performed on these potential energy surfaces (PES). More recently, new quantum calculations of the potential¹⁴ that gave a better estimate of the stationary points of the surface were incorporated into the PES used for the present calculations. This PES has also been used by Baer and collaborators¹⁵ for their centrifugal sudden (CS) approximate quantum mechanical calculations of the Li+FH reactive cross sections.

One primary objective of this paper is the discussion of the difficulties which arise in carrying out an accurate three-dimensional (3D) quantum investigation of the Li+FH reaction and a discussion of the adopted solutions. A second objective of this paper is the analysis of the results and a rationalization of some important features of the reaction dynamics of the system.

The paper is organized as follows. The new potential energy surface is discussed in Sec. II. The hyperspherical approach is illustrated in Sec. III. The construction of the surface functions and the propagation of the coupled channel (CC) scattering equations are described in Sec. IV. Detailed reactive probabilities are analyzed in Sec. V and Sec. VI contains our conclusions.

II. THE POTENTIAL ENERGY SURFACE

As already mentioned, the starting point for the construction of the potential energy surface is the set of *ab initio* values of Ref. 4. These values, calculated at a configuration interaction level, gave a barrier to reaction of 0.43 eV and an entrance channel well depth of 0.20 eV relative to the bottom of the asymptotic reactant well. However, as pointed out in Refs. 5, 7, and 14 these features cannot be reconciled with experimental findings. For this reason, before starting the fitting procedure, we scaled them to the refined estimates of Ref. 14 obtained by following the computational method of Ref. 16.

To carry out the fitting procedure, scaled *ab initio* values were mapped onto the space of the bond order (BO) variables ($\{n_i\}$) generated by exponentiating the displacement of the diatom i from the related equilibrium distance r_{ei} ($n_i = \exp[-b_i(r_i - r_{ei})]$, for the definition of BO variables and their use in dynamics studies, see also Ref. 17 and references therein). Polynomials in the BO space are appropriate functional representations of both two- (V_i^{II}) and three-body¹⁸ (V^{III}) interaction terms because they naturally die at large distances. In particular, two body terms can be expressed as polynomials of the type $V_i^{\text{II}} = \sum_{j=1}^4 a_{ij} n_i^j$. Parameters of the two-body terms were derived by forcing the reproduction of spectroscopic data of diatomic fragments (see Table I). Once the two-body components are determined, the coefficients of the polynomial $\sum_{j=0}^5 \sum_{k=0}^5 \sum_{l=0}^5 c_{jkl} n_1^j n_2^k n_3^l$ (with $j+k+l \leq 6$ and at least two indices differing from zero) approximating the three-body term were obtained by a least squares fit to the difference between the adjusted *ab initio* values and the sum of the two-body terms (see Table II where the values of c_{jkl} coefficients are given in kcal/mol, the units actually used in the FORTRAN routine). In this way, all the features of the *ab initio* potential energy values were reproduced. To fine tune the characteristics of the stationary points of the fitted surface, further corrections were introduced. In particular, the coefficients of the three-body polynomial were scaled by the factor 0.9935 to give a better reproduction of the adjusted barrier to

TABLE I. Parameters (energies in eV; distances in Å) of diatomic BO terms.

	D_{ei}	b_i	r_{ei}	a_{i1}	a_{i2}	a_{i3}	a_{i4}
LiF	5.97	0.9708	1.5639	2.3044	-2.3017	1.6903	-0.6930
FH	6.12	2.1942	0.9168	2.0781	-1.2567	0.2791	-0.1005
LiH	2.46	1.1709	1.5957	2.1512	-1.3822	0.3107	-0.0797

reaction. For the same reason, two Gaussians of the type

$$A \exp[-b_x(r_{\text{LiF}}-x)^2 - b_y(r_{\text{FH}}-y)^2 - b_z(r_{\text{LiH}}-z)^2],$$

with A , b_x , b_y , b_z , x , y , and z being, respectively, 0.1, 0.111, 0.037, 0.078, 1.6523, 1.3715, and 1.865 for the first and 1.8, 0.088, 0.096, 0.042, 1.8848, 0.9363, and 2.336 for the second Gaussian, were added. (Again, these values are given in the units actually used by the potential routine, i.e., kcal/mol for energies and Å for distances.) As a result, the reaction barrier has a height of 0.182 eV, and the entrance channel well has a depth of 0.302 eV with respect to the reactant asymptote. Moreover, two-body repulsive terms, non-negligible only in the highly repulsive part of the diatomic potentials, were added to smooth out short range spurious structure. The little remaining very short range spurious structure was found to not interfere with the calculations.

An additional reason for using BO coordinates when representing the potential energy surface of reactive processes is that the BO space is finite and inverted with respect to the physical one. Therefore, it naturally emphasizes the strong interaction region which is of primary importance for reactions and contracts the long range tail into the (0,1] interval. Energy contours of the fitted surface drawn at fixed values of the angle Φ_F , the LiFH bond angle, are shown in Figs. 1–4 as a function of the related BO variables n_{LiF} and n_{FH} . In these plots, energy contours of the BO PES taken every 0.1 eV relative to the entrance channel asymptotes are given for $\Phi_F=180^\circ$, 106° , 74° , and 45° . These contour plots show all the features of the surface (i.e., the classical endoergicity of the process, the early location of the well, the late location of the barrier, and the bent transition state geometry) as clearly as the more familiar internuclear distance plots. For example, Fig. 1 shows the contours at collinear LiFH geometries. As apparent from it, collinear encounters have a barrier to reaction slightly higher than 0.8 eV located late in the product channel and a well located in the entrance channel that is slightly deeper than 0.1 eV. Figure 2 shows the contours for $\Phi_F=106^\circ$ corresponding to the value of the entrance channel complex. In this case, the barrier to reaction, though lower than that of the collinear geometry, is still slightly higher than 0.6 eV while the entrance channel well is

TABLE II. Coefficients of the three-body BO polynomial.

C_{jkl}^a	j	k	l	C_{jkl}^a	j	k	l
0.922 405 2d+03	1	1	0	-0.201 926 8d+03	1	2	2
0.327 286 0d+03	1	0	1	0.108 576 9d+03	0	3	2
0.338 170 6d+03	0	1	1	0.368 902 4d+02	2	0	3
-0.104 864 3d+04	2	1	0	0.125 919 2d+03	1	1	3
-0.296 256 9d+03	1	2	0	-0.139 851 0d+02	0	2	3
-0.383 914 0d+03	2	0	1	-0.548 955 1d+01	1	0	4
-0.747 806 8d+03	1	1	1	-0.272 174 1d+02	0	1	4
-0.753 312 4d+03	0	2	1	-0.867 270 2d+01	5	1	0
-0.171 547 0d+03	1	0	2	0.924 372 5d+02	4	2	0
-0.213 440 7d+01	0	1	2	0.945 549 5d+02	3	3	0
0.550 848 1d+03	3	1	0	0.437 855 8d+02	2	4	0
0.113 438 2d+04	2	2	0	-0.301 289 5d+03	1	5	0
-0.116 004 2d+04	1	3	0	0.587 543 3d+02	5	0	1
0.355 739 0d+03	3	0	1	-0.764 494 2d+01	4	1	1
0.101 708 6d+02	2	1	1	-0.154 424 2d+03	3	2	1
0.696 916 0d+03	1	2	1	0.117 467 2d+01	2	3	1
0.125 887 7d+04	0	3	1	0.188 109 9d+02	1	4	1
0.519 758 2d+02	2	0	2	0.269 934 0d+03	0	5	1
0.432 801 8d+03	1	1	2	-0.380 389 7d+02	4	0	2
-0.106 210 1d+03	0	2	2	0.221 147 4d+02	3	1	2
0.547 194 2d+02	1	0	3	0.171 319 9d+03	2	2	2
-0.321 156 8d+02	0	1	3	0.670 984 5d+02	1	3	2
-0.133 351 5d+03	4	1	0	-0.299 939 5d+02	0	4	2
-0.499 358 2d+03	3	2	0	0.128 541 4d+02	3	0	3
-0.392 873 4d+03	2	3	0	0.545 717 4d+02	2	1	3
0.114 333 3d+04	1	4	0	-0.974 547 7d+02	1	2	3
-0.225 214 1d+03	4	0	1	-0.719 712 3d+01	0	3	3
0.264 176 6d+03	3	1	1	-0.137 745 4d+01	2	0	4
0.996 472 9d+02	2	2	1	-0.212 002 8d+02	1	1	4
-0.303 165 4d+03	1	3	1	0.207 108 7d+02	0	2	4
-0.991 940 8d+03	0	4	1	0.700 303 2d+00	1	0	5
0.712 358 9d+02	3	0	2	0.422 919 5d+01	0	1	5
-0.502 649 0d+03	2	1	2				

^aIn kcal/mol.

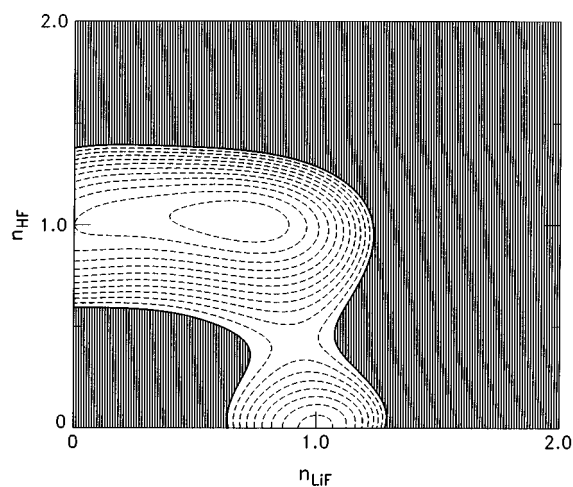


FIG. 1. Isoenergetic contours of the present Li+FH potential energy surface with the bond angle Φ_F fixed at 180° (collinear) plotted as a function of the bond order coordinates n_{LiF} and n_{HF} . The energy contour interval is 0.1 eV, and regions where the potential energy is about 1.0 eV are shaded. The energy zero is taken to be at the bottom of the asymptotic reactant well, so that the zero contour just touches the edge of the plot at $n_{LiF}=0$, $n_{HF}=1$ (see the text for discussion).

near its deepest point (about 0.3 eV). Contours taken at a value of Φ_F close to that for the transition state (74°) shown in Fig. 3 indicate a barrier to reaction that is lower than 0.2 eV high and a double well structure. The first well is located in the entrance channel and, as for the other angles already considered, is slightly more than 0.1 eV deep. The second well is located in the exit channel and is less than 0.1 eV deep with respect to the barrier or the product asymptote. The energy contours drawn at $\Phi_F=45^\circ$ (see Fig. 4) clearly show a high barrier separating the reactant and product channels.

A more detailed study of the reactive features of the PES as a function of the angle Φ_F was carried out by plotting minima and maxima of fixed angle minimum energy paths. To determine fixed angle minimum energy paths, the BO

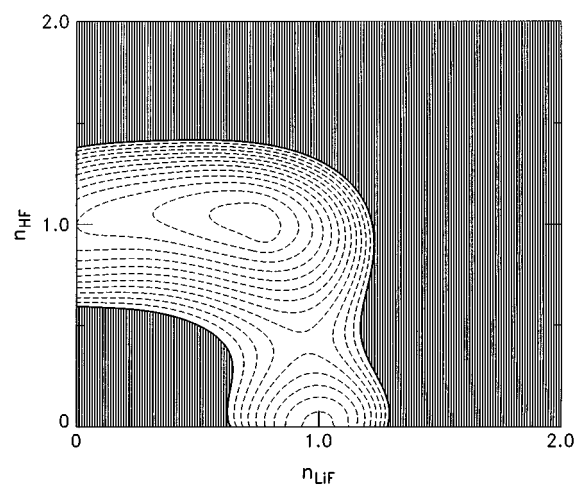


FIG. 2. As in Fig. 1 for $\Phi_F=106^\circ$.

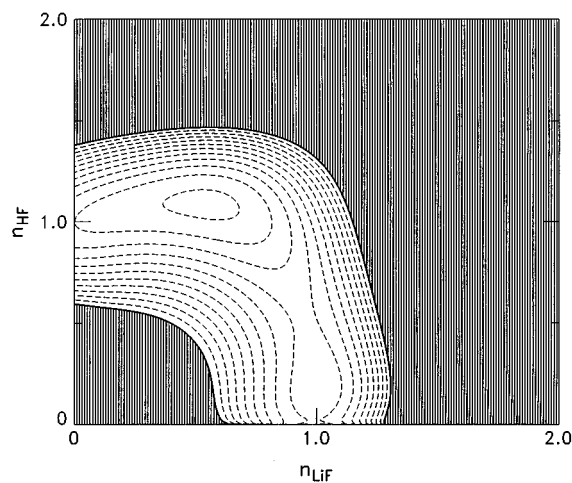


FIG. 3. As in Fig. 1 for $\Phi_F=74^\circ$.

representation gives the additional advantage of allowing the use of straight lines centered on the axes origin.¹⁹ The value of the potential energy at the stationary points is plotted as a function of the angle Φ_F in Fig. 5. The solid line, which is the early barrier height, shows a minimum at an angle around 74° and an energy of 0.182 eV. This barrier increases smoothly toward larger angles and rises rapidly toward smaller angles. An interesting detail of these plots is that for a small interval of the angle Φ_F a further barrier, located later in the exit channel, shows up. Such a barrier, shown by the heavy dashed line in Fig. 5, is higher than the previous one for a range of about 5° and leads to the formation of a small pocket about 0.087 eV deep shown by the light dashed line. The entrance channel well, 0.302 eV deep, is shown by the dashed-dotted line in Fig. 5. All these features, although shifted in energies, are also found in the unscaled *ab initio* results. They also agree with the experimental findings of Loesch and Stienkemeier.²⁰

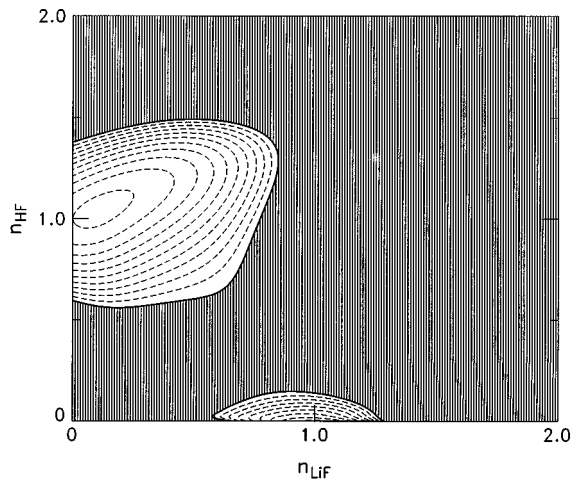


FIG. 4. As in Fig. 1 for $\Phi_F=45^\circ$.

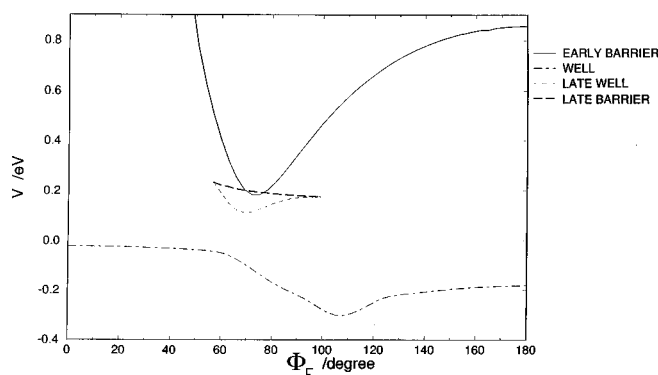


FIG. 5. Barriers and wells of the fixed angle minimum energy paths plotted as a function of the bond angle Φ_F (see the text for discussion). The dotted-dashed line is for the early well; the solid line is for the early barrier; the light dashed line is for the late well; and the heavy dashed line is for the late barrier.

III. THE HYPERSPHERICAL APPROACH

The hyperspherical formalism adopted here has been described in detail in Ref. 21. It makes use of adiabatically adjusting principal axis of inertia hyperspherical (APH) coordinates.²² In the APH formalism the three internal coordinates are ρ , θ , and χ . These can be defined in terms of the usual mass scaled Jacobi coordinates (S_τ , s_τ , and Θ_τ) as

$$\begin{aligned} \rho^2 &= S_\tau^2 + s_\tau^2, \\ \tan \theta &= \frac{[(S_\tau^2 - s_\tau^2)^2 + 4S_\tau^2 s_\tau^2 \cos^2 \Theta_\tau]^{1/2}}{2S_\tau s_\tau \sin \Theta_\tau}, \\ \sin(2\chi_\tau) &= \frac{2S_\tau s_\tau \cos \Theta_\tau}{[(S_\tau^2 - s_\tau^2)^2 + 4S_\tau^2 s_\tau^2 \cos^2 \Theta_\tau]^{1/2}}, \\ \cos(2\chi_\tau) &= \frac{S_\tau^2 - s_\tau^2}{[(S_\tau^2 - s_\tau^2)^2 + 4S_\tau^2 s_\tau^2 \cos^2 \Theta_\tau]^{1/2}}. \end{aligned} \quad (1)$$

In these coordinates the Hamiltonian is

$$H = T_\rho + T_h + T_r + T_c + V(\rho, \theta, \chi). \quad (2)$$

(The initial arrangement label of χ has been omitted because the relationship $\chi_j = \chi_i - \chi_{ji}$ makes the three different χ_j differ only in origin.) In Eq. (2) the subscripts stand for “rho”, “hypersphere,” “rotational,” and “Coriolis,” respectively, and the individual terms are given by

$$T_\rho = -\frac{\hbar^2}{2\mu\rho^5} \frac{\partial}{\partial\rho} \rho^5 \frac{\partial}{\partial\rho}, \quad (3)$$

$$T_h = -\frac{\hbar^2}{2\mu\rho^2} \left(\frac{4}{\sin 2\theta} \frac{\partial}{\partial\theta} \sin 2\theta \frac{\partial}{\partial\theta} + \frac{1}{\sin^2 \theta} \frac{\partial^2}{\partial\chi^2} \right), \quad (4)$$

$$T_r = A(\rho, \theta) J_x^2 + B(\rho, \theta) J_y^2 + C(\rho, \theta) J_z^2, \quad (5)$$

and

$$T_c = -\frac{i\hbar \cos \theta}{\mu\rho^2 \sin^2 \theta} J_y \frac{\partial}{\partial\chi}, \quad (6)$$

with $A(\rho, \theta)$, $B(\rho, \theta)$, and $C(\rho, \theta)$ being defined as

$$A(\rho, \theta) = \frac{1}{\mu\rho^2(1 + \sin \theta)},$$

$$B(\rho, \theta) = \frac{1}{2\mu\rho^2 \sin^2 \theta}, \quad (7)$$

$$C(\rho, \theta) = \frac{1}{\mu\rho^2(1 - \sin \theta)}.$$

This Hamiltonian, although more complicated than when written in Jacobi coordinates, is simpler than those obtained when using most other curvilinear coordinates.

To solve the scattering problem using a CC technique, the wave function for a given total angular momentum \mathbf{J} is expanded in products of Wigner rotation functions $D_{\Lambda M}^J$ of the three Euler angles (α , β , and γ), surface functions Φ of the two internal hyperangles (θ and χ), and (initially unknown) functions ψ of the hyperradius ρ . The ρ range is divided into a number of sectors. For each sector i a set of surface functions $\Phi_i(\theta, \chi; \rho_i)$ is calculated at the center, ρ_i , of the sector. These surface functions, which serve as a local basis set, are independent of ρ on a given sector but change between sectors and have been variously denoted “sector adiabatic” or “diabatic by sectors” by different authors.

Therefore, when the total angular momentum \mathbf{J} is set equal to zero, the first computational step to accomplish is the solution of the following bound state equations

$$\left(T_h + \frac{15\hbar^2}{8\mu\rho_i^2} + V(\rho_i, \theta, \chi) - \mathcal{E}_i(\rho_i) \right) \Phi_i(\theta, \chi; \rho_i) = 0 \quad (8)$$

in θ and χ to evaluate the fixed ρ surface functions.

To see the nature of the surface functions and the equation they satisfy, it is particularly useful to analyze fixed ρ cuts of the PES that appear in Eq. (8). These cuts are usually plotted as stereographic projections of the surface of internal coordinate sphere onto a Cartesian plane whose x and y coordinates are defined as

$$x = \tan \frac{\theta}{2} \cos \chi, \quad y = \tan \frac{\theta}{2} \sin \chi. \quad (9)$$

These plots, given in Figs. 6–9, show the variation of the potential energy as the triangle formed by the three atoms distorts to assume different arrangement geometries for a fixed value of the hyperradius. In particular, as θ goes from zero at the center of the figure ($x=y=0$) to $\theta=90^\circ$ at the periphery, the triangle flattens from one for which the two principal moments of inertia in the triatomic plane are equal into a straight line. As χ goes from 0° to 360° (circling counter clockwise around the figure starting from the positive x axis) all possible arrangements are described twice for reasons discussed elsewhere.²¹

At large ρ values (see Fig. 6 for $\rho=20a_0$), the graph shows that the different energetically allowed asymptotic regions of the potential are well separated and confined to small portions of the plane. This is due to the polar nature of the hyperspherical coordinates. As ρ increases, the angles θ and χ span an increasingly larger interval of the internuclear distances.

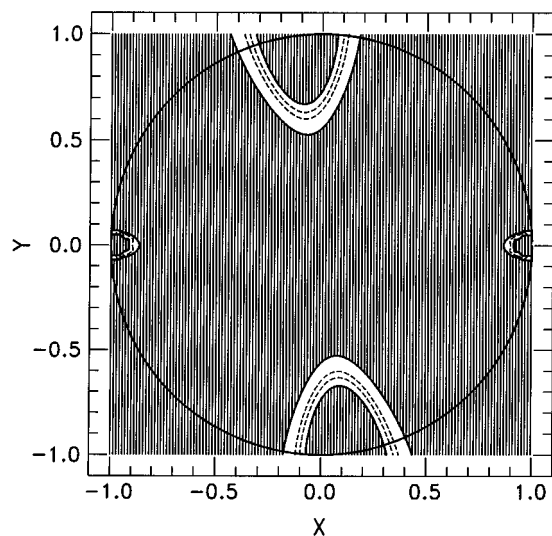


FIG. 6. Stereographic projection of a contour plot of the Li+FH potential energy surface as a function of the APH hyperangles θ (the circle radius) and χ (the circle angle) with the hyperradius fixed at $\rho=20a_0$. The dotted contour is at 0.2 eV, and regions above 1.5 eV are shaded. The small features located near $x=\pm 1$ and $y=0$ show the reactant Li+FH arrangement channel; the larger features near $x=0$, $y=\pm 1$ show the product LiF+H arrangement channel. The closed F+LiH channel does not appear on this plot. Only the encircled area has physical meaning.

At intermediate ρ values, the arrangement channels, though still separate, fill up more of the fixed ρ plane (see Fig. 7 for $\rho=8a_0$). At ρ values around the transition state (see Fig. 8 for $\rho=5.14a_0$) the reactant Li+FH and the product LiF+H channels partly merge, and there is a saddle point between them. Near the saddle there is a small well that corresponds to the fixed ρ cut of the pocket shown in Fig. 5. At shorter ρ values (see Fig. 9 for $\rho=4.5a_0$) the distinction among different channels is no longer evident at all, and the PES is getting repulsive.

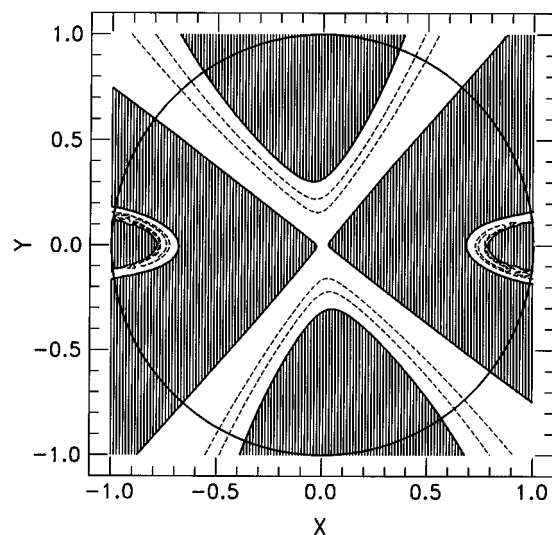


FIG. 7. As in Fig. 6 for $\rho=8a_0$, except that the dotted contours are at 0 and 0.2 eV.

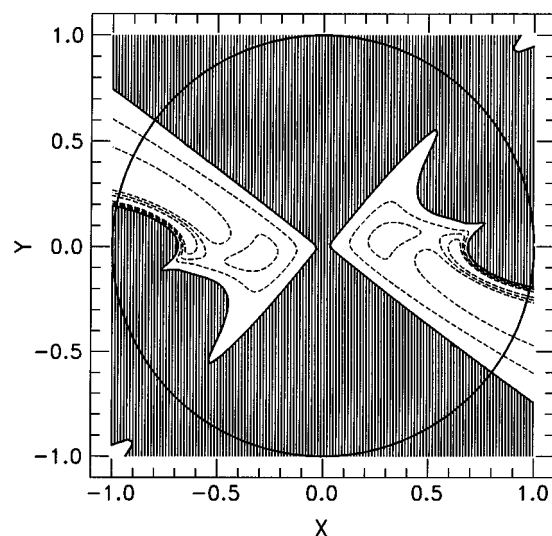


FIG. 8. As in Fig. 6 for $\rho=5.14a_0$, the distance of the transition state. The dotted contours are at 0, 0.2, and 0.4 eV. Vestiges of the repulsive cores of each channel are visible; the large shaded areas near $\chi=\pm\pi/2$ are due to LiF, the small shaded areas near $\chi=0$ and π are due to HF; and the intermediate sized shaded areas near $\chi=\pi/6$ and $7\pi/6$ are due to the LiH channel (closed). The system gets from reactant to product by passing (with χ near 0 or π) as θ decreases, from the entrance channel well over the barrier into the late well.

One suggestive way of giving compact representations of the PES is to plot it in two variables while adjusting the third one to minimize the potential. These “relaxed variable” representations were first introduced using Cartesian projections of Jacobi coordinates,²³ and extended later to hyperspherical coordinates by allowing either a hyperangle or the hyperradius to relax.²⁴ Plots of the Li+FH PES obtained by relaxing the θ hyperangle have been given in Ref. 24. Here, Fig. 10 shows the one obtained by relaxing the hyperradius

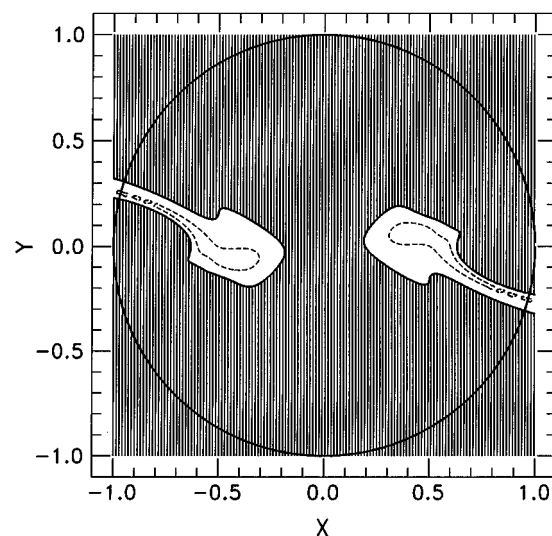


FIG. 9. As in Fig. 6 for $\rho=4.5a_0$. The dotted contour is at 0.2 eV.

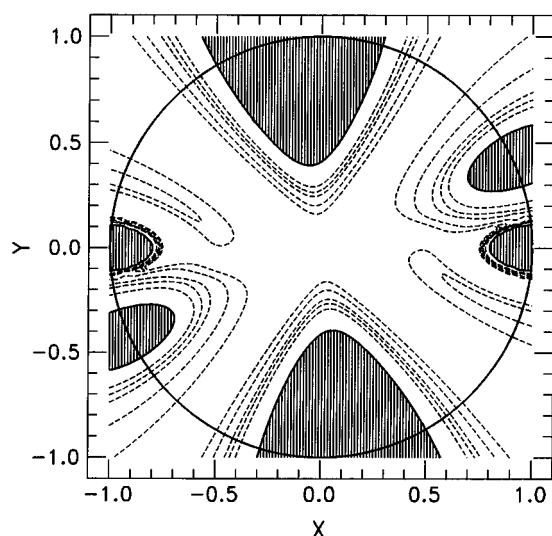


FIG. 10. As in Fig. 6 for the relaxed ρ representation. Energy contours have been taken at 0.35, 0.70, 1.42, 1.93, and 2.8 eV. Regions above 10.0 eV are shaded. See the text for discussion.

in the range $4.5a_0 - 7a_0$. It shows clearly the bent transition state separating the reactant and product arrangement channels.

IV. CONSTRUCTION OF SURFACE FUNCTIONS AND PROPAGATION

To carry out quantitatively accurate dynamical calculations the surface functions Φ , the solutions of Eq. (8) on the two-dimensional domains exemplified by the fixed ρ plots of Figs. 6–9, need to be constructed. When we first began work on the LiFH system^{21,25} we used a finite element method (FEM) to solve Eq. (8). A key step of the FEM is the generation of a mesh that will give all the energetically accessible eigenfunctions accurately using a minimum number of points. Unfortunately, as apparent from Figs. 6–9, these eigenfunctions become extremely localized at some ρ values, and it is impractical to make use of a homogeneous mesh. A heterogeneous grid of nodes was prepared starting from a regular frame of quadrangular elements each involving nine nodes. Then, additional points were inserted in the regions where the potential is deeper by halving the grid step and repeating the process a sufficient number of times. Although this technique can create arbitrarily dense meshes localized in those regions of the PES where more points are needed, it finds a limitation in the difficulty of the FEM solver to deal with rapidly varying grids. This implies that, to give an accurate description of the eigenfunctions needed, one still needs an excessively large number of points. In practice, to obtain accurate eigenvalues and surface functions at moderate ρ values we had to construct grids of up to 6000 nodal points.

To illustrate the FEM surface functions and meshes for the Li+FH reaction, perspective plots of a few surface functions calculated at $\rho=10a_0$ using a 6000 node mesh are shown in Figs. 11–15. All the surface functions shown in

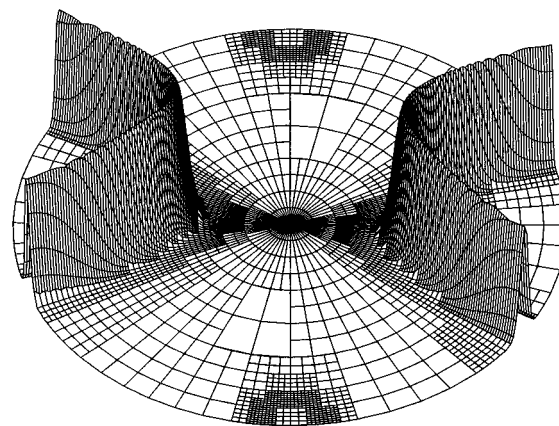


FIG. 11. Plot of the lowest-energy surface function at $\rho=10a_0$. The surface function is confined inside the LiF product channel. The vibrational and the rotational components have the structure of the $v'=0$ and $j'=0$ LiF wave function. See the text for discussion of the orientation of Figs. 11–15.

Figs. 11–14 are confined in the product LiF+H arrangement, and, at this moderately large ρ value, they have the typical shape of the isolated LiF diatom wave functions, so that one can identify them by counting nodes. One finds the vibrational state by counting nodes along χ at $\theta=90^\circ$, i.e., along the border of the circle, and the rotational state by counting the nodes encircling the arrangement channel. For example, Fig. 11 is the ground state $v=0$, $j=0$ LiF function.

On the other hand, at the same value of ρ , Fig. 15 shows the lowest-energy surface function in the reactant Li+FH arrangement. Although this function is clearly confined inside the reactant Li+FH channel, it dies on the side of the channel facing the LiH+F channel (to allow a better perspective view of the surface function structure, the locations of the channels in Figs. 11–15 have been reflected through $\chi=0$ and then rotated by $\pi/2$ along χ with respect to the origin of the stereographic projections of Figs. 6–10). This means that the function has *not* yet achieved the form of the asymptotic $v=0$, $j=0$ HF function and is strongly rotationally hindered even at $\rho=10a_0$. This rotational hindering

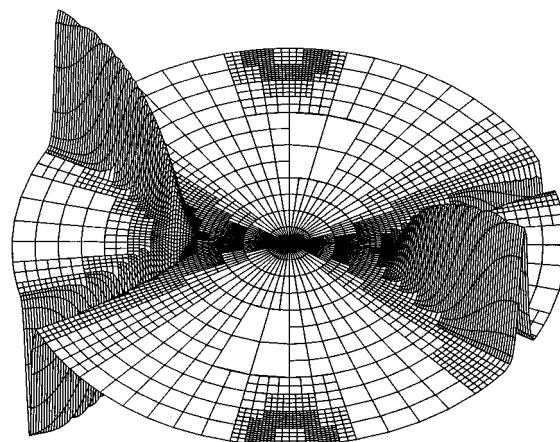


FIG. 12. As in Fig. 11 for $v'=0$ and $j'=1$.

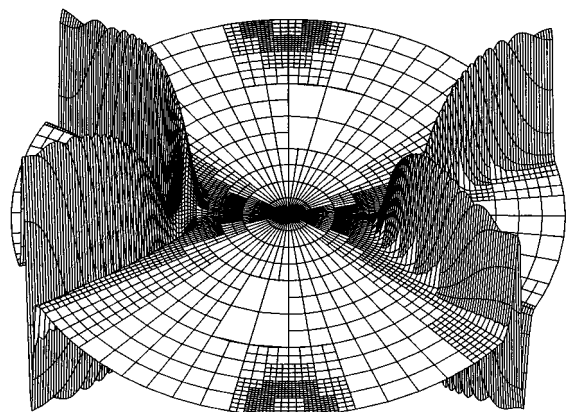


FIG. 13. As in Fig. 11 for $v'=1$ and $j'=1$.

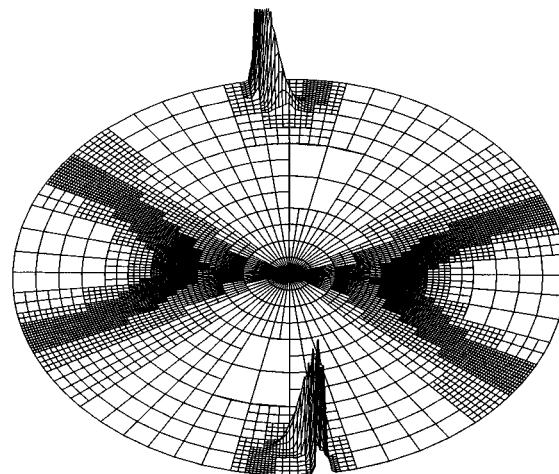


FIG. 15. Plot of the lowest-energy surface function at $\rho=10a_0$ that is localized in the reactant arrangement channel.

means that the value of ρ to which one must propagate before reaching the asymptotic region must be larger than $\rho=10a_0$.

Surface functions calculated at smaller ρ values are either confined in a single channel or spread over both reactant and product channels. In any case, they lose the typical structure of asymptotic functions as illustrated in Figs. 16 and 17 where the first and the fifth surface functions calculated at $\rho=5.14a_0$ (the value of the hyperradius at which the transition state occurs) are shown. In particular, the surface function shown in Fig. 16 is confined in what is the vestige of the Li+FH channel and is associated with a bound state supported by the entrance channel well. For this reason, this surface function does not contribute directly to the reactive flux. On the contrary, the surface function shown in Fig. 17 has components located on both sides of the barrier and thus has and mixes reactantlike and productlike properties.

At ρ values larger than $10a_0$, the FEM approach became so demanding that we chose to adopt a different method, namely, the analytical basis method²⁶ (ABM) recently developed by some of us. The ABM approach is not only ideally suited for large ρ calculations but also has been shown to

work well at medium and short distances when its parameters are chosen properly. In fact, the ABM was the only method used to calculate the surface functions used in the CC propagation calculations of the present paper; because of its efficiency and simplicity; it was used over the full range of ρ .

In the ABM approach, the surface functions are expanded in terms of rotation-vibration functions of the three sets of Delves coordinates. The vibrational basis in the f th arrangement consists of harmonic oscillator functions of an “anharmonic variable,” z_f , which distorts the space to allow for anharmonicities.²⁶ z_f is related to the Delves hyperangle ϑ_f via

$$z_f = a_f \tan \vartheta_f - \frac{b_f}{\tan \vartheta_f} + c_f. \quad (10)$$

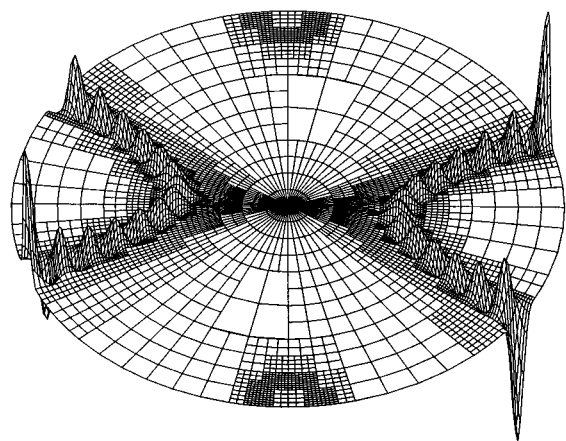


FIG. 14. As in Fig. 11 for $v'=0$ and $j'=26$.

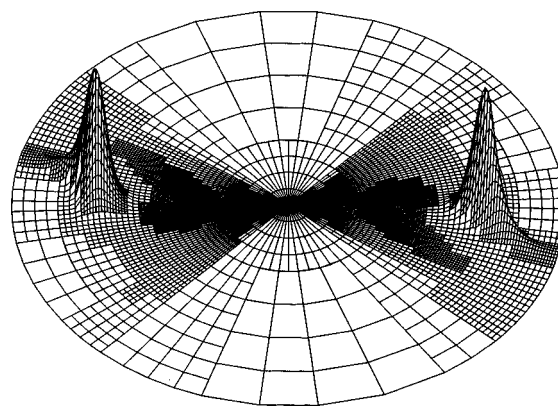


FIG. 16. Plot of the lowest-energy surface function at $\rho=5.14a_0$. This function is confined inside the reactant channel. This and Fig. 17 are oriented the same as Fig. 8.

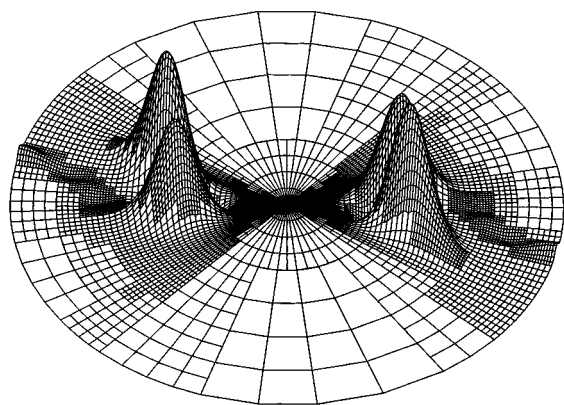


FIG. 17. Plot of the fifth-energy surface function at $\rho=5.14a_0$. This function has amplitude in both the reactant and the product channels.

The extent of the distortion is controlled by the three parameters in this equation, and these are determined by requiring the oscillator basis functions to behave approximately like Morse functions. Since the present calculations were carried out when the ABM was in its developing stage, the definitions of some parameters differ from those given in Appendix A of Ref. 26. The definitions that differ are

$$a_f = \cos^5 \vartheta_{mf} \left(g_{2f}^{1/2} + \frac{g_{3f}}{6g_{2f}^{1/2}} \sin \vartheta_{mf} \right), \quad (11)$$

$$b_f = \sin^4 \vartheta_{mf} \cos \vartheta_{mf} \left(g_{2f}^{1/2} - \frac{g_{3f}}{6g_{2f}^{1/2}} \cos \vartheta_{mf} \cot \vartheta_{mf} \right), \quad (12)$$

where

$$g_{2f}^{1/2} = C_{pf} \rho_{pf} [\mu(\omega_{ef} - \omega_{ef} x_{ef})]^{1/2}, \quad (13)$$

$$\frac{g_{3f}}{g_{2f}^{1/2}} = -g_{2f}^{1/2} \rho_{pf} A_{nf} (2\mu\omega_{ef} x_{ef})^{1/2}, \quad (14)$$

ρ_{pf} is the greater of ρ and $1.1s_{mf}$,

$$\vartheta_{mf} = \sin^{-1}(s_{mf}/\rho_{pf}), \quad (15)$$

$$C_{pf} = C_{\alpha f} + F_{\alpha f} e^{-B_{\alpha f} \rho_{pf}}, \quad (16)$$

and

$$s_{mf} = r_{xf} r_{ef} / d_f. \quad (17)$$

The values of the parameters in these equations used in the present calculations are given in Table III in atomic units. Their meanings are either the same as in Ref. 26, or they are simply scaling and fitting parameters.

As implied by the v_{\max} and j_{\max} values in Table III, the ABM calculations of the present paper used a total of 277 primitive basis functions. Integrals between them were evaluated using different numerical quadratures. At ρ values larger than $6a_0$ the quadratures were performed in the arrangement channel Delves space.²⁶ At ρ values smaller than $6a_0$ the quadratures were performed in the APH space.²⁶ In this case, θ was partitioned into two sectors (0,0.80) and (0.80, $\pi/2$), containing, respectively, 20 and 40 grid points,

TABLE III. Parameters for the ABM calculations.

Arrangement	Li+FH	F+LiH	H+LiF
mass (amu)	7.016 003	18.998 4032	1.007 825 03
ω_e (a.u.)	0.018 855 57	0.006 404 61	0.004 147 81
$\omega_e x_e$ (a.u.)	0.000 409 52	0.000 105 71	0.000 036 127
r_e (a_0)	1.732 517	3.015 437 2	2.955 276
v_{\max}	4	0	5
j_{\max}	14	3	32
n_{hermt}	50	50	50
n_{legn}	50	50	50
C_{α}	0.91	0.91	0.947
r_x	1.1	1.075	1.035
F_{α}	0	0	2.526
B_{α}	0	0	0.385
A_n	1	0.9	1.05

while χ was divided into the five sectors $(-\pi/2, -0.89)$, $(-0.89, -0.25)$, $(-0.25, 0.25)$, $(0.25, 0.89)$, and $(0.89, \pi/2)$. The surface functions $\Phi_i(\theta, \chi; \rho_i)$ were then determined by direct diagonalization of the Hamiltonian of Eq. (8). To obtain the matrix elements needed in the propagation step of the calculations, these surface functions were calculated at 230 sectors centered at the ρ values determined using the expression

$$\rho_i = [\rho_{\min} + (i-1)\Delta\rho_1](1 + \Delta\rho_2)^{i-1}, \quad (18)$$

where $\rho_{\min} = 3.5a_0$, $\Delta\rho_1 = 0.025a_0$, and $\Delta\rho_2 = 5.839\ 827\ 930\ 082\ 4 \times 10^{-3}$.

The resulting surface function eigenvalues are plotted in Fig. 18. In the investigated energy range, the asymptotic curves show the rotational states of the ground vibrational state of the FH reactant superimposed on the more narrowly spaced rotational levels of several of the lower vibrational states of the LiF product. It should be noted that the curves shown in Fig. 18 are connected from one sector to another in energy order; i.e., they are *adiabatic* curves, and they show numerous avoided crossings. We also note that one can connect the points based on the largest overlaps of the surface functions of one sector with those of the next.²⁷ The resulting *diabatic* curves connect more smoothly at intermediate distances, have a more single channel nature, and allow one to

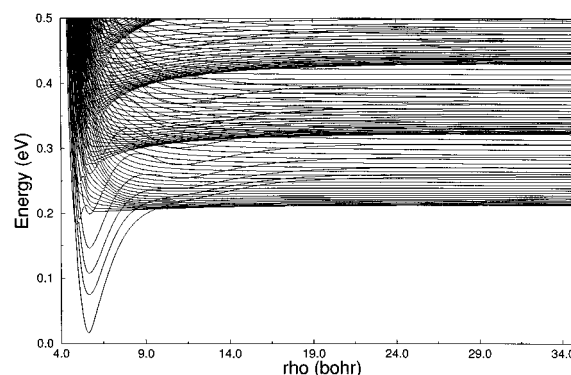


FIG. 18. Adiabatic surface function eigenvalues plotted as a function of the hyperradius.

more easily see to which arrangement channel a given curve most strongly connects. They are discussed more later in the paper. Both the diabatic curves and Fig. 18 clearly show that the lower curves connecting to the product H+LiF arrangement channel at large distances tend to remain quite constant in energy down to quite short distances. This is consistent with the lack of distortion in Figs. 11–14. Those correlating with the higher vibrational states of LiF show a decrease in energy at smaller ρ values before becoming repulsive at small ρ . On the contrary those connecting to the reactant Li+FH channel show a richer structure. In particular, as ρ decreases from initially large values, the curves lowest in energy show first a small attraction, then a barrier associated with the orbiting of Li around the FH molecule and then a well associated with the entrance channel LiFH complex followed by a repulsive region. Those at higher energy gradually absorb the well into the repulsive wall because of the growing importance of the orbiting contribution. At very short ρ values both types of curves lose their single channel nature.

The coupled differential equations of the coupled channel (CC) method that result from the use of the surface functions have the following form

$$\left(\frac{\partial^2}{\partial \rho^2} + \frac{2\mu E}{\hbar^2}\right)\psi_t(\rho) = \frac{2\mu}{\hbar^2} \sum_{t'} \langle \Phi_t(\theta, \chi; \rho_i) | H_i | \Phi_{t'}(\theta, \chi; \rho_i) \rangle \psi_{t'}(\rho), \quad (19)$$

where the internal Hamiltonian here is

$$H_i = T_h + T_c + \frac{15\hbar^2}{8\mu\rho^2} + V(\rho, \theta, \chi). \quad (20)$$

The numerical integration of the 277 coupled equations was carried out from $\rho = 3.5a_0$ to $\rho = 35a_0$ using a logarithmic derivative method with 24 propagation steps per smallest propagation wavelength.²⁸ Once the solution had been propagated to $35a_0$, the asymptotic analysis was performed²¹ and the **S** matrix elements evaluated. The convergence of the calculations has been tested by varying the surface function basis set from 200 to 277 functions.

The number of quadrature points were varied to produce surface function eigenenergies accurate to 4 significant energies. At two energies the number of propagation steps were increased. This resulted in a change of the probabilities only in the third significant figure. The resulting probabilities are accurate to within a percent at the nonresonant lower energies with the error increasing to about 10% at the higher energies. The heights of the resonance peaks are less accurate than that since a slight change in the basis can shift a given energy onto or off a narrow resonance. Higher energies would require a larger primitive basis set in the ABM calculations.

V. REACTIVE PROBABILITIES: DISCUSSION

A. Energy dependence

As already pointed out in Ref. 29, the reactive probability of this reaction has no threshold. This is because the zero point energy of the reactants is larger than that of the prod-

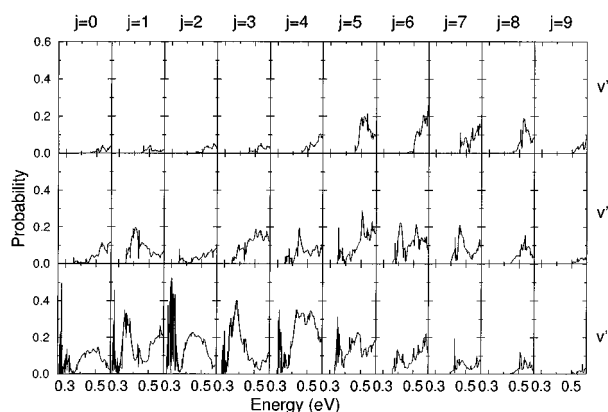


FIG. 19. Reactive probabilities summed over all open product j' states for $v=0$ to $v'=0$ (lowest row), $v'=1$ (center row), and $v'=2$ (upper row), for given reactant j values (j increases going from left to right) plotted as a function of the total energy.

ucts to make the reaction quantally exoergic and, as the reaction proceeds, the zero point energy evolves smoothly from the Li+FH asymptotic value to the LiF+H one, almost completely absorbing the potential energy barrier.

In Fig. 19, typical reactive probabilities for initial $v=0$ and different initial j values (different columns) to find v' ranging from 0 to 2 (from the lowest to the highest row) summed over the product rotational states j' are plotted as a function of total energy E . (Primed quantities are used for products, unprimed for reactants.) As we already pointed out in Ref. 29, all the reactive probabilities for transitions from $v=0, j=0$ of the reactants to the different j' values of the product ground vibrational state seem to show a common resonant (sharp peaks) and oscillating (slow background oscillations) structure. The plot of those $v=0, j=0$ to $v'=0$ reactive probabilities summed over all j' states is shown here in the lower left hand corner of Fig. 19. As can be easily seen from the figure, the probability summed over j' shows the same oscillatory and resonant structure as the individual detailed probabilities plotted in Fig. 2 of Ref. 29 implying that this feature is truly common to all the detailed probabilities when the reactants are in the ground vibrotational state. Following the indications given there, we attempted to interpret both the resonant and the slower oscillatory structure using simple models.³⁰

B. Narrow resonances

Obviously, the rationalization of the narrow resonance structures in the 3D quantum results of this noncollinear Li+FH reaction is far more complex than it was for the symmetric collinear reactions considered before.³¹ We proceeded as follows. In the left-hand panel of Fig. 20, we have plotted the resonant energy range of the *diabatic* curves that connect to the product LiF+H arrangement. Superimposed on these as horizontal lines are the energy eigenvalues of the bound states that are obtained in calculations in which each of these curves is treated independently and all coupling between them is neglected. In the right-hand panel, we have

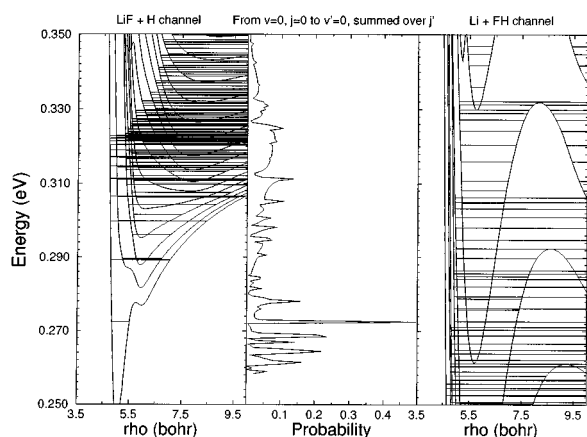


FIG. 20. Comparison of the energies of the reactive resonances with those of the bound states supported by the wells in the channel diatomic curves defined in Sec. IV. The bound states of the product curves are in the left panel; those of the reactants are in the right panel. Resonant energies of the $v=0, j=0$ to $v'=0$, summed over j' reactive probabilities are in the center panel.

plotted the same energy range of the diabatic curves that connect to *reactants* and their eigenvalues when treated as uncoupled. In the center panel of Fig. 20, we have replotted the lower left-hand panel of Fig. 19 with its axes reversed and its energy scale expanded to match the other parts of the figure. The reader who has a straight edge can readily discover that every sharp resonance peak in the central panel is correlated with one of the energy levels in the right panel. (This is more quickly obvious when a transparency of one of the panels is laid over the other.) For the lower energy peaks, the energies match within the linewidths of the resonances. The higher energy resonance peaks are shifted to slightly but increasingly lower energies than the corresponding energy levels. This happens because the simple eigenvalues of the uncoupled curves must necessarily be upper bounds to the true resonance energies given by the accurate scattering results in the central panel which include all coupling. It should be noted, however, that not every energy level in the right panel has a corresponding peak in the reactive probability. This means that some of these levels are either not accessed, give rise to resonances too broad to be visible, or give rise to resonances that decay only to reactants and do not contribute to the reactive probability.

No such correlation is found between the resonances and the energy levels of the left panel. The most that can be claimed there is a weak qualitative correlation of the average background reaction probability with the density of states in the left panel.

Thus, it appears that the sharp resonance structures in the low-energy reaction probabilities are Feshbach resonances due to the system getting trapped in metastable states in the entrance channel well region. It also appears that the peaks with the narrower widths and larger amplitudes are those trapped behind the lower, wider barrier separating them from the long-range part of the entrance arrangement channel.

C. Broader oscillations

Ignoring the sharp structures in several of the lower panels in Fig. 19, we see that the background has broad oscillations at high energy which get narrower and narrower as the energy decreases. Somewhat similar structures have previously been found in collinear and fixed-collision-angle infinite order sudden (IOS) calculations.^{9,32,33} However, those structures had a different spacing than the present ones, and those in IOS calculations tend to disappear when the results are averaged over the collision angle.

To get a simple interpretation of the present oscillations, we construct an extremely simple model. Beginning from Eq. (19) we assume that we have transformed the CC equations to a diabatic representation, so that the coupling occurs in the potential terms. Then, we consider just two states, one of which connects to the desired incident reactant state (such as $v=0, j=0$) and the other of which represents a collection of product rotational states which are assumed to be closely spaced and to surround the energy of the incident state, so that they can be considered to have the same asymptotic energy as it. With these assumptions, the resulting pair of equations has the same form as those of the very first IOS papers,³⁴ and their formulas can be used directly. Furthermore, to make the model completely analytically soluble, we take the potential to be an infinite square well inside some turning point ρ_t , zero outside ρ_t+d , and between those points to be the constant 2×2 matrix,

$$V = \begin{pmatrix} -D & fD \\ fD & f^2D \end{pmatrix}. \quad (21)$$

Thus, this potential, in qualitative consistency with the curves of Fig. 18 has a square well of depth D in the reactant channel, an off-diagonal coupling that is a fraction f of the well depth, and much shallower square well in the product channel. This particular form is chosen for convenience and to keep a minimum number of parameters. The resulting reaction probability is³⁴

$$P = 4U_{22}^2 U_{12}^2 \sin^2(\eta_2 - \eta_1), \quad (22)$$

where \mathbf{U} is the transformation that diagonalizes \mathbf{V} , and the η_i are phase shifts. For the present model,

$$U_{22}^2 U_{12}^2 = f^2 / (1 + f^2)^2 \quad (23)$$

and

$$\eta_2 - \eta_1 = \left(\frac{2\mu}{\hbar^2} \right)^{1/2} \{ (E - E_{\text{thresh}})^{1/2} - [E - E_{\text{thresh}} + D(1 + f^2)]^{1/2} \} d. \quad (24)$$

Using the threshold energy (0.255 eV) of the ground state reactants and choosing $D=0.076$ eV, $f=0.2$, and $d=3.5a_0$ as physically reasonable values (see Fig. 18) of the fitting parameters, one gets the reaction probability shown in Fig. 21. Comparing it with the lower left panel of Fig. 19, one sees that it nearly quantitatively reproduces the amplitudes and positions of both the maxima and minima of the two higher energy oscillations. However, there is so much narrower resonance structure in the lower energy part of the lower left panel of Fig. 19 and its enlargement in the middle

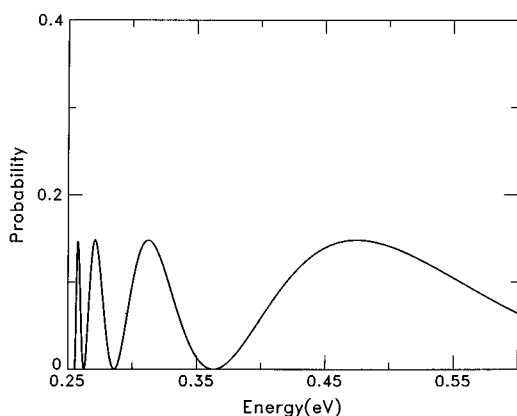


FIG. 21. Oscillatory structure obtained from a very simple model of the reactive probabilities for $v=0$, $j=0$, $v'=0$ and summed over j' . See the text for discussion.

panel of Fig. 20 that it is difficult to see how many of the slower oscillations it might have. (Figure 21 has two between 0.255 and 0.29 eV.) However, if one looks across the lower panels of Fig. 19, one sees that as the initial j increases, it pushes the threshold upward, pushes the higher energy oscillations off the right side of the plot, and begins to split up the lower energy highly structured region until by $j=3$, it has clearly split into two peaks, and by $j=4$, the two peaks corresponding to the two lowest energy peaks in Fig. 21 are the only two slow oscillations remaining on the plot in the lower center of Fig. 19.

The broadening of the lower energy oscillations as j increases is also consistent with the observation from Fig. 18 that the diabatic curves correlating with the higher j states of the reactants have shallower wells; they have repulsive centrifugal potentials which eventually dominate over the wells as j increases.

Thus, from the remarkably good correspondence of this simple model to the accurate results, it appears that the slower oscillations in these reaction probabilities are due to quantum interference between the reactant and product channels and to the fact that the reactant channels see a much stronger potential well than the product channels.

Although this extremely simple model is able to account for the j dependence of the $v=0$ to $v'=0$ reaction probabilities, one sees from the upper two rows of Fig. 19 that no such simple structure is seen in the transitions to $v'>0$. For small j these are endoergic transitions with a threshold independent of j . Further, for all j , it appears that these transitions involve a mechanism that is beyond the simplest sudden model just described.

A final comment needs to be made on the dependence of the reactive probability on j . In Fig. 22, the reaction probabilities from reactants in $v=0$ to the different v' states are plotted vs j at three total energies near the upper end of the energy range of the calculations. One notes from this figure that the dependence on j is more regular than one might have expected from scanning from left to right along a given row of Fig. 19. One sees some alternations with j which shift with energy, and also that, as the energy increases, the higher

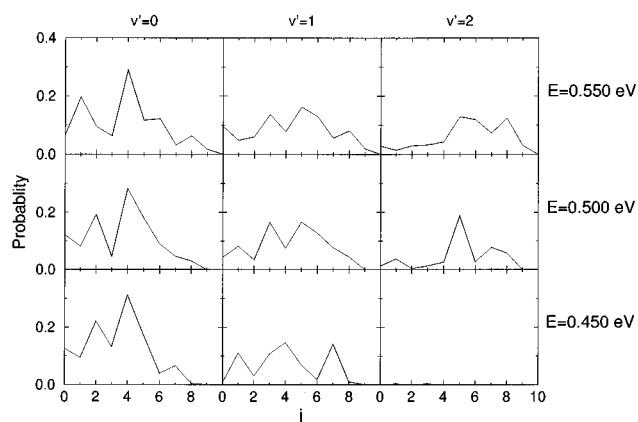


FIG. 22. Reactive $v=0$ to $v'=0$ (left-hand column), $v'=1$ (center column), and $v'=2$ (right-hand column), probabilities summed over all open product j' states plotted as a function of j at $E=0.45$, 0.50 , and 0.55 eV from the lower to the upper panel.

j and v' states become open and begin to contribute to the reaction. Also, since these calculations were performed with $J=0$, there is the restriction $j=l\leq b$ with b being the classical impact parameter. Therefore, the curves of Fig. 22 behave like opacity functions and die at large j . In addition, the fact that these opacity functions are not large at small j values and tend to increase with j before dying off makes their shape different from the “hard sphere” (i.e., the stepwise) shape of the opacities of the other metal plus hydrogen halide heavy-heavy-light reactions.³⁵

D. Product distributions

Other quantities that aid in understanding this reaction are the final state distributions of the products at fixed energies. Although calculated only for $J=0$, so that $\mathbf{l}=-\mathbf{j}$, these distributions still contain a great deal of information about the reactive dynamics of the system.

We first discuss the product vibrational distributions (PVD's). PVD's summed over all j' for reactants in $v=0$ are given in Fig. 23 for three different values of E ($E=0.45$, 0.50 , and 0.55 eV going from the left to the right-hand side columns of Fig. 23) and several values of j (j increases from 0 to 9 going from the lower to the upper row). Though the total reactivity is definitely smaller than unity, the shapes of the PVD's are always unimodal, a behavior also given by the $v+1$ rule of Franck-Condon models.³⁶⁻³⁸ Other common features of the different plots are the shift of the PVD peak to higher v' values as energy increases, leading to somewhat inverted distributions, and the spreading of the distribution over a more extended set of states (i.e., to an increase of the average vibrational energy of products). Similar behavior has been found in collinear calculations performed for the Mg+FH system³⁷ and in calculations for other systems³⁸ in which there is a sudden change in the shape of the potential about the minimum energy path as the system passes the saddle point.

The product rotational distributions (PRD's) are shown in Fig. 24 for three energies. These PRD's show a rather

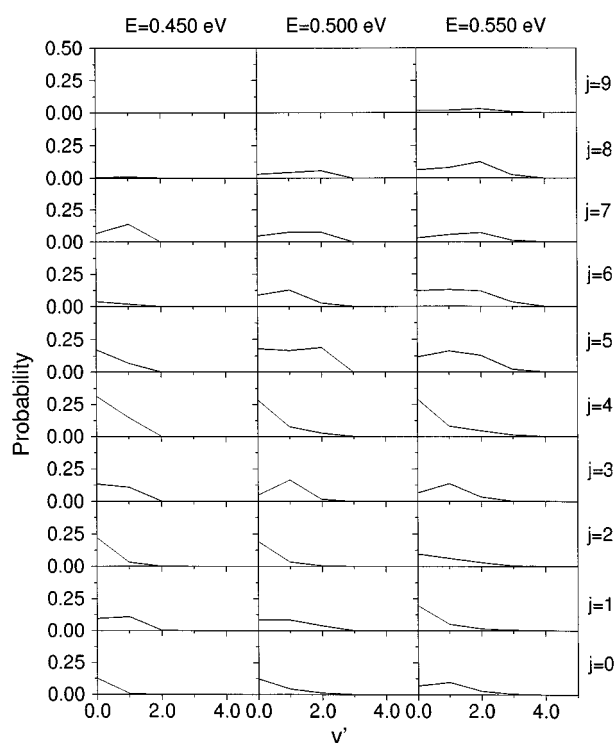


FIG. 23. Product vibrational distributions (probability vs v') calculated at $E=0.45$ eV (left-hand column), 0.50 eV (center column) and 0.55 eV (right-hand column) and given reactant j values (j increases going from lower to upper rows) summed over all open product rotational states.

structured shape with some tendency for even-odd alternation and some propensity to favor even j' over odd j' . However, this propensity is far from complete: For a given initial j , it often reverses as the energy changes, and at a given E , it also often reverses as a function of initial j . In fact, in a single plot it sometimes reverses as a function of j' . We do not presently know the cause of these alternations.

If one ignores this alternation structure, and looks at the overall behavior with j' , one sees that, in most of the panels of Fig. 24, the probability starts off at $j'=0$ about as large as it ever gets and tapers off to zero at moderately large j' values. Since, as already mentioned, for $J=0$ one has $l'=-j'$ for the rotor and orbital angular momenta, these PRD's can be interpreted as product opacity functions (that is, plots vs the product impact parameter). This tapering off to zero without an intermediate maximum means that in the product valley the system senses a repulsive potential. (For example, a hard sphere opacity function is constant for small l' and then drops to zero for large l' .) This behavior, common to other light-heavy-heavy reactions³⁹ (as is the reverse H+LiF reaction), contrasts with the behavior seen for the reactants in Fig. 22 where the attractive well in the reactant valley gives rise to maxima at intermediate j values.

VI. CONCLUSIONS

We have reported an *ab initio* study of the Li + FH \rightarrow LiF + H reaction. The potential energy surface used is based on both new and older *ab initio* calculations; a bond

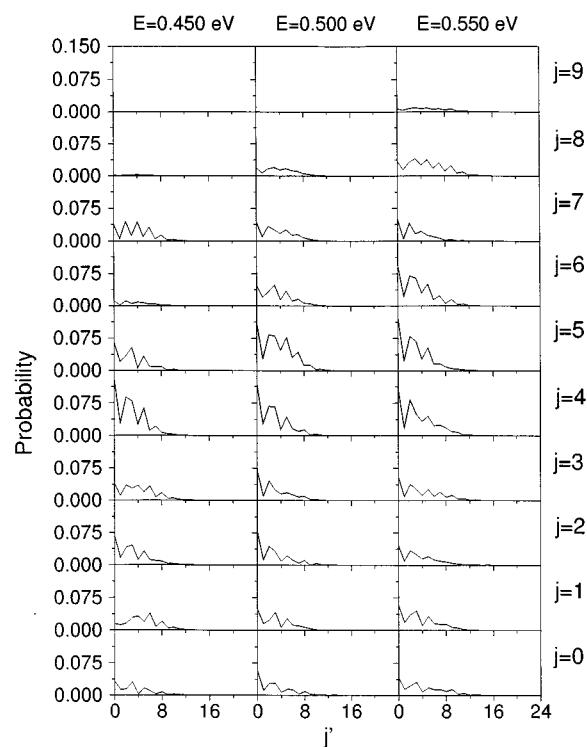


FIG. 24. Product rotational distributions (probability vs j') calculated at $E=0.45$ eV (left-hand column), 0.50 eV (center column) and 0.55 eV (right-hand column) and given reactant j values (j increases going from lower to upper rows) to the ground product vibrational state ($v'=0$).

order fit of it was described and the parameters given. Accurate 3D quantum reactive scattering calculations were carried out at zero total angular momentum using the APH formalism, and the resulting reaction probabilities were presented and discussed. Narrow spikes in the probabilities at low energies were found to be Feshbach resonances due to trapping in binding effective potential curves that are energetically open in the interaction region but closed at large hyperradius. Broader oscillations in the background $v=0$ to $v'=0$ reaction probabilities were shown with a very simple model to be due to quantum interference between states that connect to reactants and sense an attractive well in the entrance valley and states that connect to products and sense little attraction. Transitions to $v'>0$ do not show such simple behavior. The product vibrational distributions are unimodal and show somewhat inverted distributions. The product rotational distributions show some tendency to even-odd alternations in the final rotational state j' , but the alternations shift with energy and initial rotational state j .

ACKNOWLEDGMENTS

This work was performed under the auspices of the U.S. Department of Energy under the Laboratory Directed Research and Development Program at Los Alamos. Financial support was also given by NATO (Grant No. CRG 920051), CNR(I), and ENEA(I).

- ¹C. H. Becker, P. Casavecchia, P. W. Tiedemann, J. J. Valentini, and Y. T. Lee, *J. Chem. Phys.* **73**, 2833 (1980).
- ²H. J. Loesch, A. Ramscheid, E. Stenzel, F. Stienkemeier, and B. Wustenbecker, in *Physics of Electronic and Atomic Collisions*, edited by W. R. McGillivray, I. E. McCarty, and M. Standage (Adam Hilger, Bristol, 1992), p. 579; H. J. Loesch, E. Stenzel, and B. Wustenbecker, *J. Chem. Phys.* **95**, 3841 (1991); H. J. Loesch and F. Stienkemeier, *ibid.* **98**, 9570 (1993); **99**, 9598 (1993).
- ³G. G. Balint-Kurti and R. N. Yardley, *Faraday Discuss. Chem. Soc.* **62**, 77 (1977).
- ⁴M. M. L. Chen and H. F. Schaefer, III, *J. Chem. Phys.* **72**, 4376 (1980).
- ⁵S. Carter and J. N. Murrell, *Mol. Phys.* **41**, 567 (1980).
- ⁶E. Garcia and A. Laganà, *Mol. Phys.* **52**, 1115 (1984).
- ⁷A. Laganà, O. Gervasi, and E. Garcia, *Chem. Phys. Lett.* **143**, 174 (1988).
- ⁸J. M. Alvarino, P. Casavecchia, O. Gervasi, and A. Laganà, *J. Chem. Phys.* **77**, 6341 (1982); A. Laganà, M. L. Hernandez, and J. M. Alvarino, *J. Mol. Struct. (Theochem)* **107**, 87 (1984); *Chem. Phys. Lett.* **106**, 41 (1984); J. M. Alvarino, M. L. Hernandez, E. Garcia, and A. Laganà, *J. Chem. Phys.* **84**, 3059 (1986); J. M. Alvarino, M. L. Hernandez, M. Basterrechea, and A. Laganà, *Mol. Phys.* **59**, 559 (1986).
- ⁹J. M. Alvarino, O. Gervasi, and A. Laganà, *Chem. Phys. Lett.* **87**, 254 (1982); A. Laganà, J. M. Alvarino, and M. L. Hernandez, and M. Basterrechea, *J. Mol. Struct. (Theochem)* **120**, 187 (1985).
- ¹⁰I. Noorbachta and N. Sathyamurthy, *J. Am. Chem. Soc.* **104**, 1766 (1982); *J. Chem. Phys.* **76**, 6447 (1982); *Chem. Phys. Lett.* **93**, 432 (1982); *Chem. Phys.* **77**, 67 (1983).
- ¹¹H. J. Loesch, *Chem. Phys. Lett.* **104**, 213 (1986); H. J. Loesch and M. Hoffmeister, *Faraday Trans. II* **85**, 1253 (1989).
- ¹²A. Laganà and E. Garcia, *Chem. Phys. Lett.* **139**, 140 (1987); A. Laganà, E. Garcia, and O. Gervasi, *J. Chem. Phys.* **89**, 7238 (1988); M. Baer, E. Garcia, A. Laganà, and O. Gervasi, *Chem. Phys. Lett.* **158**, 140 (1987) A. Laganà, X. Gimenez, E. Garcia, A. Aguilar, and J. M. Lucas, *ibid.* **176**, 280 (1991).
- ¹³D. L. Miller and R. E. Wyatt, *J. Chem. Phys.* **86**, 5557 (1987).
- ¹⁴P. Palmieri and A. Laganà, *J. Chem. Phys.* **91**, 7302 (1989).
- ¹⁵M. Baer, H. J. Loesch, and I. Last, *Chem. Phys. Lett.* **219**, 372 (1994).
- ¹⁶M. J. Frisch, J. S. Binkley, and H. F. Schaefer, *J. Chem. Phys.* **81**, 1882 (1984).
- ¹⁷E. Garcia and A. Laganà, *Mol. Phys.* **56**, 521 (1985).
- ¹⁸E. Garcia and A. Laganà, *Mol. Phys.* **56**, 529 (1985); Dini, *Tesi di Laurea*, Perugia (1986).
- ¹⁹A. Laganà, *J. Chem. Phys.* **95**, 2216 (1991); A. Laganà, G. Ferraro, E. Garcia, O. Gervasi, and A. Ottavi, *Chem. Phys.* **168**, 341 (1992).
- ²⁰H. J. Loesch and F. Stienkemeier, *J. Chem. Phys.* **99**, 9598 (1993).
- ²¹R. T Pack and G. A. Parker, *J. Chem. Phys.* **87**, 3888 (1987); **90**, 3511 (1989).
- ²²R. T Pack, *Chem. Phys. Lett.* **108**, 333 (1984).
- ²³A. Laganà, *Comp. Chem.* **4**, 137 (1980).
- ²⁴V. Aquilanti, A. Laganà, and R. D. Levine, *Chem. Phys. Lett.* **158**, 87 (1989); A. J. C. Varandas, *ibid.* **138**, 455 (1987).
- ²⁵G. A. Parker, R. T Pack, A. Laganà, J. D. Kress, and Z. Bacic, in *Supercomputer Algorithms for Reactivity, Dynamics and Kinetics of Small Molecules*, edited by A. Laganà (Kluwer, Dordrecht, 1989), p. 105; R. T Pack, G. A. Parker, and A. Laganà, *Farad. Disc. Chem. Soc.* **91**, 386 (1991).
- ²⁶R. T Pack and G. A. Parker, *J. Chem. Phys.* **98**, 6883 (1993).
- ²⁷R. B. Walker, and G. A. Parker (unpublished).
- ²⁸B. R. Johnson, *J. Chem. Phys.* **67**, 4086 (1977); **69**, 4678 (1978).
- ²⁹G. A. Parker, R. T Pack, and A. Laganà, *Chem. Phys. Lett.* **202**, 75 (1993).
- ³⁰V. Aquilanti, S. Cavalli, and A. Laganà, *Chem. Phys. Lett.* **93**, 174 (1982); V. Aquilanti, S. Cavalli, G. Grossi, and A. Laganà, *J. Mol. Struct. (Theochem)* **107**, 95 (1984).
- ³¹V. Aquilanti, S. Cavalli, and A. Laganà, *Chem. Phys. Lett.* **93**, 179 (1982); A. Laganà, M. L. Hernandez, and J. M. Alvarino, *J. Mol. Struct. (Theochem)* **107**, 87 (1984).
- ³²R. B. Walker, Y. Zeiri, and M. Shapiro, *J. Chem. Phys.* **74**, 1763 (1981).
- ³³G. G. Balint-Kurti, S. P. Mort, F. Gogtas, A. Laganà, and O. Gervasi, *J. Chem. Phys.* **99**, 9567 (1993).
- ³⁴T. P. Tsien and R. T Pack, *Chem. Phys. Lett.* **6**, 54 (1970); R. T Pack, *ibid.* **14**, 393 (1972).
- ³⁵C. A. Leach, A. A. Tsekouros, P. H. Vaccaro, R. N. Zare, and D. Zhao, *Faraday Discussion Chem. Soc.* **91**, 183 (1981).
- ³⁶M. Baer, *J. Chem. Phys.* **62**, 4545 (1975).
- ³⁷A. Laganà, M. Paniagua, and J. M. Alvarino, *Chem. Phys. Lett.* **168**, 441 (1990).
- ³⁸A. Laganà, *J. Chem. Phys.* **86**, 5523 (1987); A. Laganà, E. Garcia, and J. M. Alvarino, *Novo Cimento D* **12**, 1539 (1990).
- ³⁹J. N. L. Connor, A. Laganà, A. F. Turfa, and J. C. Whitehead, *J. Chem. Phys.* **75**, 3301 (1981).